

Reconstructing and Simulating Dynamic 3D Objects with Mesh-adsorbed Gaussian Splatting

Shaojie Ma
Zhejiang University

Yawei Luo*
Zhejiang University

Yi Yang
Zhejiang University

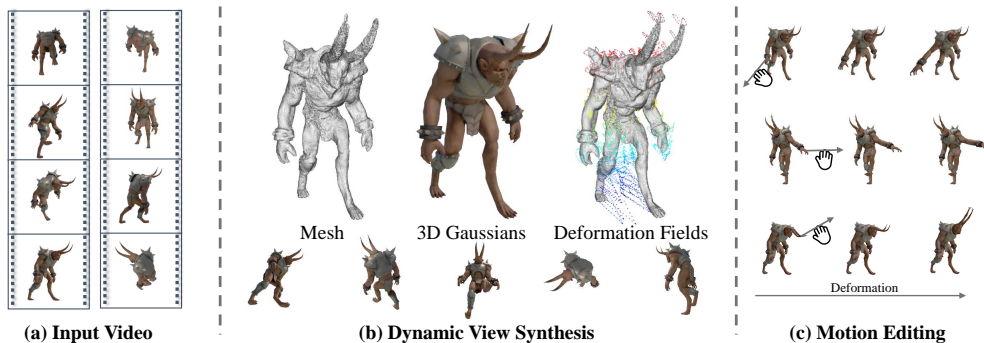


Figure 1: We propose the Mesh-adsorbed Gaussian Splatting (MaGS), a unified framework for reconstructing and simulating a dynamic 3D object from a monocular video.

Abstract

3D reconstruction and simulation, while interrelated, have distinct objectives: reconstruction demands a flexible 3D representation adaptable to diverse scenes, whereas simulation requires a structured representation to model motion principles effectively. This paper introduces the Mesh-adsorbed Gaussian Splatting (MaGS) method to resolve such a dilemma. MaGS constrains 3D Gaussians to hover on the mesh surface, creating a mutual-adsorbed mesh-Gaussian 3D representation that combines the rendering flexibility of 3D Gaussians with the spatial coherence of meshes. Leveraging this representation, we introduce a learnable Relative Deformation Field (RDF) to model the relative displacement between the mesh and 3D Gaussians, extending traditional mesh-driven deformation paradigms that only rely on ARAP prior, thus capturing the motion of each 3D Gaussian more precisely. By joint optimizing meshes, 3D Gaussians, and RDF, MaGS achieves both high rendering accuracy and realistic deformation. Extensive experiments on the D-NeRF and NeRF-DS datasets demonstrate that MaGS can generate competitive results in both reconstruction and simulation.

1 Introduction

The human visual system can simultaneously capture the 3D appearance (reconstruction) and infer the probable motions (simulation) of dynamic objects from a monocular video. In contrast, computer vision and graphics typically treat 3D reconstruction and simulation as distinct tasks. Over the years,

*Corresponding author.

¹Project page: <https://wvac.github.io/MaGS-page/>.

various reconstruction methods have emerged [22, 23, 41, 42, 27]. These methods represent the geometry and appearance of a 3D scene from multi-view images, either implicitly or explicitly, and subsequently render photo-realistic novel views based on the 3D representation. Neural Radiance Fields (NeRF)[26], an implicit method, utilizes volume rendering techniques to bridge 2D and 3D spaces. To expedite NeRF, approaches such as neural hashing [29] and tri-plane [10, 7] representations have been introduced. Explicit methods represent a 3D scene more concretely using such as 3D points as rendering primitives, with representative methods including PointRF [52] and Pulsar [17]. More recently, 3D Gaussian Splatting (3DGS) has demonstrated significant improvements in rendering quality and speed [15, 3], and has been extended to 4D scene reconstruction [43, 48, 47, 25]. These representations, whether explicit or implicit, do not impose substantial prior information on the reconstructed object, enabling flexible application across various scenes.

The simulation utilizes reconstruction results for motion editing [33, 12, 46], ray tracing rendering [35], and other applications [24, 44, 6]. Due to the lack of structural or physical priors, such as skeletons, simulating the raw reconstruction results often appear unrealistic. To address this, some methods introduce explicit representations to enhance simulation capabilities [50, 46, 54, 13]. For instance, Huang *et al.*[11] applied control points as learnable handles to guide deformation more structurally. In specific cases like human body simulation, parametric models such as SMPL [49, 20] are commonly used. Some approaches aim to integrate spatial continuity priors by introducing explicit mesh representations. Guedon and Waczynska [9, 40] employed a hybrid mesh and 3DGS representation to achieve more natural editing of static objects. Recently, Liu *et al.* [18] proposed a dynamic mesh Gaussian method to extend hybrid representations for simulating dynamic objects, thus enhancing their simulation capabilities.

3D reconstruction and simulation, while interrelated, have distinct objectives: reconstruction requires a flexible 3D representation adaptable to diverse scenes, whereas simulation necessitates a structured representation to model deformation policies effectively. This dual requirement poses significant challenges for a unified framework. To address this, we introduce the Mesh-adsorbed Gaussian Splatting (MaGS) method. MaGS constrains 3D Gaussians to hover on the mesh surface, creating a hybrid mesh-Gaussian 3D representation that combines the rendering flexibility of 3D Gaussians with the spatial coherence of meshes. Leveraging this representation, we further propose a learnable Relative Deformation Field (RDF) to model the relative movement between the mesh and Gaussians, in addition to the mesh deformation itself. These designs distinguish MaGS from other methods that typically use the anchored and fixed mesh-Gaussian representation [18, 40, 9]: By allowing relative displacement between the mesh and 3D Gaussians through the learnable RDF, MaGS bypasses the trade-off between rendering accuracy and deformation rationality during dynamic object reconstruction. On the simulation side, MaGS extends the as-rigid-as-possible (ARAP) [38] prior within meshes to capture a relative motion of each 3D Gaussian, thus handling more complex deformations. By joint optimizing meshes, 3D Gaussians, and RDF, MaGS achieves both high rendering accuracy and realistic deformation. Extensive experiments on the D-NeRF and NeRF-DS datasets demonstrate that MaGS outperforms current methods in both reconstruction and simulation, significantly reducing floating points and artifacts. In this regard, MaGS presents a new paradigm for a unified reconstruction and simulation framework.

To summarize, our contributions are as follows:

- We propose an innovative mesh-adsorbed 3D Gaussians representation that combines the rendering flexibility of 3D Gaussians with the spatial coherence of meshes, enabling the unification of reconstruction and simulation tasks.
- We introduce the mesh-adsorbed 3D Gaussian Splitting (MaGS) method, which jointly optimizes meshes, 3D Gaussians, and their relative deformation field via video rendering. MaGS achieves both high rendering accuracy and realistic deformation of dynamic objects.

2 Related Work

2.1 Neural Rendering for Dynamic Scenes

Since its inception by Mildenhall *et al.* [26], NeRF has driven rapid advancements in 3D scene reconstruction and novel view synthesis using differentiable rendering. Gao *et al.* [8] extended NeRF to dynamic scenes, underscoring dynamic scene reconstruction as a pivotal area in NeRF-

related research and a burgeoning field of interest. Several studies have explored augmenting NeRF with temporal positional encoding to render dynamic scenes at various time points [33, 39]. Other works have focused on integrating temporal information with voxel representations to significantly reduce training time [5, 19]. Additionally, some research has adopted k -plane representations to optimize temporal and spatial dimensions [7, 10, 2, 37]. Park et al. [30] utilized geometric priors for regularization and implemented motion fields, while Park et al. [31] projected motion into hyperspace, enhancing the expressive power and physical interpretability of deformation fields. Notably, Yan et al. [45] enhanced rendering accuracy by modeling specular reflections.

More recently, 3DGS [15] has gained increasing attention. It significantly improves rendering speed compared to NeRF while providing a clearer geometric interpretation through point clouds. Dynamic field research has also been applied to 3DGS, with studies discussing the use of deformation fields for representing dynamic scenes [48, 14, 43].

2.2 Neural Rendering Enhanced by Explicit Priors

Recent studies have explored effective deformation capabilities by introducing explicit priors. NeRF-Editing [50] integrates NeRF with mesh deformation using ARAP [38], while NeuMesh [46] directly incorporates neural fields onto meshes for superior deformation editing. SuGar [9] utilizes Poisson reconstruction to *bind* Gaussian point clouds to mesh and optimizes them simultaneously. GaMeS [40] introduces pseudo-mesh, and designs a mesh Gaussian *binding* algorithm for deformation editing. However, these approaches have yet to be extended to dynamic scenarios. In recent research, parametric models are combined to fit scene deformations, exemplified by Qian et al. [34], Chen et al. [4], Moreau et al. [28] for human body deformation scene modeling. SC-GS [11] employs sparse control points for Gaussian point cloud deformation. DG-Mesh [18] enhances 3DGS and mesh integration by mapping Gaussian points to mesh facets with Gaussian-Mesh *Anchoring* for uniformity and improved mesh optimization. MaGS distinguishes itself from the above-mentioned methods [18, 40, 9] by allowing the relative mesh-GS deformation.

3 Preliminaries

3D Gaussian Splatting (3DGS) [15] employs millions of learnable 3D Gaussians to explicitly map spatial coordinates to pixel values, enhancing rendering efficiency and quality via a rasterization-based splatting approach. Each 3D Gaussian is represented by a Gaussian function parameterized by mean μ and variance Σ , which can be defined as:

$$G(x) = e^{-\frac{1}{2}(x-\mu)^T \Sigma^{-1}(x-\mu)}. \quad (1)$$

3DGS also introduces the vector $s \in R^3$ that controls the scaling, and the vector $q \in R^4$ that controls the rotation. These components are then transformed into the corresponding rotation matrix R and scaling matrix S . To optimize the covariance matrix, Σ is decomposed into:

$$\Sigma = R S S^T R^T. \quad (2)$$

Additionally, each Gaussian retains an opacity value σ to adjust its influence in the rendering and is associated with spherical harmonic coefficient sh to achieve a view-dependent appearance. Gaussian rasterization pipeline, which can project 3D Gaussian to 2D and render each pixel using the following 2D covariance matrix Σ' :

$$\Sigma' = J V \Sigma V^T J^T, \quad (3)$$

where W is viewing transformation, and J is the Jacobian of affine projective transformation.

When rendering 2D pixel u , the function to calculate color is as follows:

$$C(u) = \sum_{i \in N} T_i \alpha_i c_i, \quad (4)$$

$$\alpha_i = \sigma_i e^{-\frac{1}{2}(u-\mu_i)^T \Sigma'(u-\mu_i)},$$

where T_i symbolizes transmittance, defined as $\prod_{j=1}^{i-1} (1 - \alpha_j)$, and c_i denotes Gaussian color along the ray, and μ_i represents the 2D projection coordinates of the 3D Gaussians.

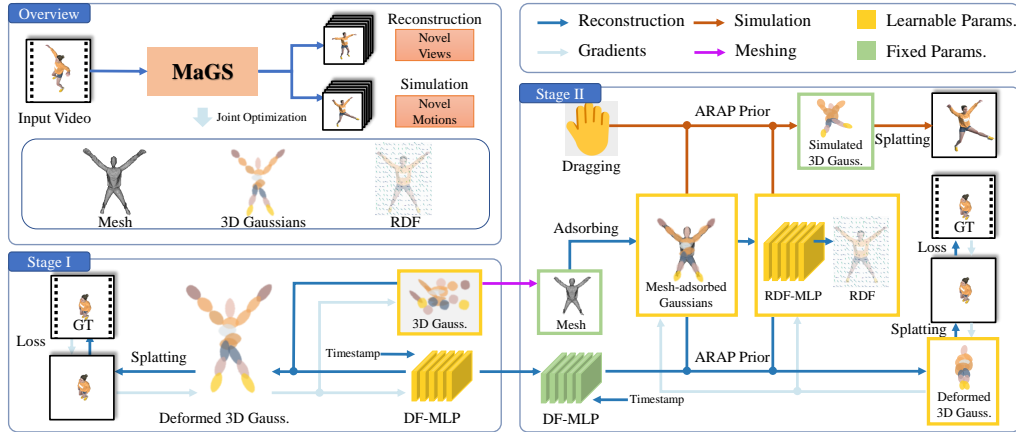


Figure 2: The MaGS pipeline comprises two stages. In Stage I, we randomly initialize 3D Gaussians and utilize a deformation fields MLP (DF-MLP) to generate a deformation field for these Gaussians. The deformed Gaussians are rendered using splatting, and the loss between the rendered view and the ground-truth video frame is computed to optimize both the Gaussian parameters and DF-MLP. At the end of Stage I, we use Marching Cubes [21] to extract a static mesh from the 3D Gaussians. In Stage II, the parameters of the DF-MLP are copied from Stage I and kept fixed, while Mesh-adsorbed Gaussians are initialized by adsorbing random 3D Gaussians to the mesh. In each iteration, the timestamp is fed into the DF-MLP and combined with the ARAP algorithm to deform the Mesh-adsorbed Gaussians. The ARAP-deformed Mesh-adsorbed Gaussians are then forwarded to a Relative Deformation Fields MLP (RDF-MLP) to compute the RDF. The Gaussians on the mesh then hover according to the RDF, resulting in the final deformed output for rendering. In this process, the parameters of RDF-MLP, mesh and 3D Gaussians are jointly optimized based on the rendering loss. For simulation, Mesh-adsorbed Gaussians are deformed using Dragging and ARAP deformation, calibrated by RDF to achieve the final deformation result. The simulation result can be directly rendered due to the 3D Gaussian representation.

4 Methodology

4.1 Stage I: Mesh Extraction and Deformation Field Estimation

Figure 2 depicts a pipeline overview of MaGS. In stage I, we begin by modeling the coarse shape and deformation of a dynamic object in a monocular video. Specifically, we randomly initialize 3D Gaussians and utilize a deformation field to represent the temporal variations of each Gaussian. An MLP (dubbed DF-MLP) is employed to predict such deformation field from the initial frame (0-th frame) to any subsequent frame (t -th frame). For the initial Gaussian G_g at time 0, we define a 3D Gaussian as $\{G_g(T=0) : \mu_g, q_g, s_g, \sigma_g, c_g\}$. At time t , the deformation field assists in predicting the changes:

$$(\delta\mu, \delta q, \delta s, \delta\sigma, \delta c) = \mathcal{D}(\mathcal{E}_p(\mu_g), \mathcal{E}_t(t)), \quad (5)$$

where μ_g represents the mean of the Gaussian at time 0, \mathcal{E} represents the function that embedding timestamp and coordinates. The predicted deformations are then applied to the initial 3D Gaussian to obtain the Gaussian at time t , resulting in $\{G_g(T=t) : \mu_g + \delta\mu, q_g \times \delta q, s_g + \delta s, \sigma_g + \delta\sigma, c_g + \delta c\}$. The deformed Gaussians are rendered using splatting, and the loss between the rendered view and the ground-truth video frame is computed to optimize both the Gaussian parameters and DF-MLP.

To establish a coarse mesh from the 3D Gaussians, we adopt the method proposed by Guédon and Lepetit [9]. This involves estimating a point cloud from depth maps rendered by the 3D Gaussians and subsequently applying the Marching Cubes algorithm for reconstruction [21].

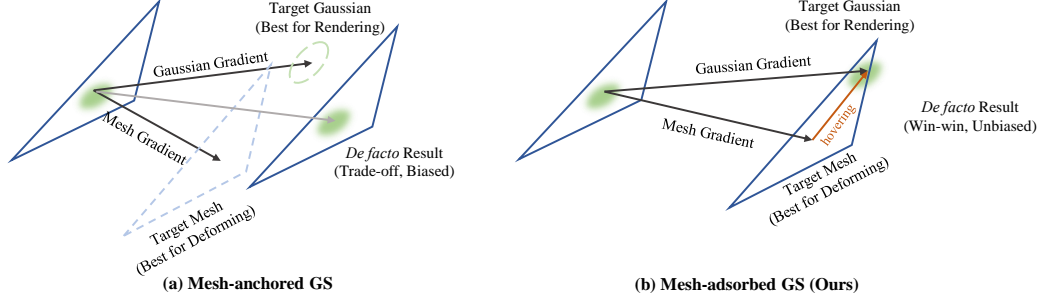


Figure 3: To our knowledge, all existing methods [18, 40, 9] that integrate 3D Gaussians with mesh representations anchor each Gaussian to a mesh facet in a fixed manner, preventing any **relative displacement** between the mesh and 3D Gaussians despite mesh deformations. Consequently, when optimizing both mesh and Gaussian parameters simultaneously, the actual positions of the 3D Gaussians and the mesh can deviate from their intended positions, as illustrated in (a). This misalignment compromises the optimization process, negatively impacting rendering accuracy and deformation rationality. MaGS addresses this by allowing 3D Gaussians to hover on the mesh surface (implemented with RDF), facilitating joint optimization for mesh and Gaussians, as shown in (b).

4.2 Stage II: Mesh-adsorbed Gaussian Splatting

4.2.1 Mesh-adsorbed Gaussians

To establish a connection between meshes and 3D Gaussians, we introduce the Mesh-adsorbed 3D Gaussian representation. We utilize a triangular mesh foundation, where each mesh facet m of the initial mesh M comprises vertices $v_{1..3} \subset \mathbb{R}^3$. For the original Mesh-adsorbed Gaussians that have not been deformed, we initialize them to ensure that the center of the 3D Gaussian is located on the mesh, and we use the following formula to calculate μ of the Gaussian g adsorbed on m :

$$\mathcal{F}(x) = \frac{1}{e^{-x} + 1},$$

$$\mu = \frac{\vec{v}_1 \times \mathcal{F}(\alpha_1) + \vec{v}_2 \times \mathcal{F}(\alpha_2) + \vec{v}_3 \times \mathcal{F}(\alpha_3)}{\mathcal{F}(\alpha_1) + \mathcal{F}(\alpha_2) + \mathcal{F}(\alpha_3)}. \quad (6)$$

Here, $\alpha_{1..3} \subset \mathbb{R}^3$ dictates the Gaussian’s placement on the mesh, which is a learnable parameter initialized with random values. This representation ensures that the Gaussian is adsorbed near the center of the mesh and iteratively changes its relative position through training. During optimization, α is optimized to precisely position the 3D Gaussians to improve rendering accuracy.

Unlike other methods, MaGS allows the 3D Gaussians to **hover on** rather than **anchor to** a facet when the mesh deforms. The motivation of such a design is detailed in Figure 3. To achieve adaptive hovering, our method calculates position-dependent value Δ_α and Δ_μ to represent the hovering of the Gaussians on the mesh when the mesh deforms using RDF, which will be explained detailed in 4.2.3. For deformed Mesh-adsorbed Gaussians, we should consider hovering when calculating the μ of the adsorbed Gaussians. The specific formula is as follows:

$$\alpha'_i = \alpha_i + \Delta_{\alpha_i},$$

$$\mu = \frac{\vec{v}'_1 \times \mathcal{F}(\alpha'_1) + \vec{v}'_2 \times \mathcal{F}(\alpha'_2) + \vec{v}'_3 \times \mathcal{F}(\alpha'_3)}{\mathcal{F}(\alpha'_1) + \mathcal{F}(\alpha'_2) + \mathcal{F}(\alpha'_3)} + \Delta_\mu. \quad (7)$$

Additionally, the shape of the Gaussians changes during deformation. We update the scaling of g based on the area change ratio of m before and after deformation. Specifically, our algorithm computes the changes of s_g of the Mesh-adsorbed Gaussians as follows:

$$s'_g = s_g * \frac{|(\vec{v}'_2 - \vec{v}'_1) \times (\vec{v}'_3 - \vec{v}'_1)|}{|(\vec{v}_2 - \vec{v}_1) \times (\vec{v}_3 - \vec{v}_1)|}, \quad (8)$$

where v and v' represent the vertices of m before and after deformation respectively, and s'_g represents the scaling parameter of g after deformation.

For the rotation q_g , we compute orthogonal bases for the mesh before and after deformation using Gram-Schmidt process [1]:

$$\mathcal{O} = \text{GramSchmidt}(\vec{v}_2 - \vec{v}_1, \vec{v}_3 - \vec{v}_1, (\vec{v}_2 - \vec{v}_1) \times (\vec{v}_3 - \vec{v}_1)) \quad (9)$$

We then calculate the rotation R^* that trans the orthogonal basis \mathcal{O} before deformation relative to the basis \mathcal{O}' after deformation. The updated Gaussian rotation q'_g is given by $q'_g = q_g R^*$.

Since the entire process is differentiable, we can jointly optimize the mesh and 3D Gaussians adsorbed on mesh through backpropagation of rendering errors.

4.2.2 Local-Rigid Deformation (Mesh Deformation)

The deformation information obtained in Stage I, presented in form of the weights in DF-MLP, is relatively rough and inaccurate. Due to the lack of constraints, the deformation network is not smooth at certain positions, which will cause points at certain positions to be discontinuous during deformation. Using this information to directly guide Mesh-adsorbed Gaussians to deform cannot achieve good results. To solve this problem, we first apply Poisson disk sampling [51]² to the current mesh of Mesh-adsorbed Gaussians to obtain a set of uniformly distributed handles. During deformation, we forward the handles and target timestamp t into DF-MLP to obtain their corresponding deformed positions. We then use ARAP to calculate the target locations of the remaining other points.

The coordinates of the handles, both before and after deformation, are then input into the ARAP algorithm. The ARAP method computes the deformed mesh by minimizing the distortion of the mesh facets while allowing for local rigid transformations. This is achieved by solving a series of optimization problems that preserve the relative distances between neighboring vertices as much as possible. Specifically, the ARAP energy function is defined as:

$$E_{\text{ARAP}}(V') = \sum_{i=1}^n \sum_{(i,j) \in E} \omega_{ij} \|(V'_i - V'_j) - R_i(V_i - V_j)\|^2, \quad (10)$$

where V and V' are the original and deformed vertex positions, respectively, E represents the set of edges, ω_{ij} are weights set to 1, and R_i is the best-fitting rotation matrix for vertex i .

Through this method, we reduce the dependence on the deformation network, which only provides rough deformation information, thus reducing the impact of its error on the final result.

4.2.3 Relative Deformation Fields (3D Gaussians Deformation)

While applying ARAP deformation allows the mesh to achieve relatively natural motion, ARAP relies on the assumption of local rigidity. In real-world scenarios, objects often do not adhere strictly to this assumption, resulting in discrepancies that can reduce accuracy during rendering. To address this issue, we introduce a learnable relative deformation field, which enables more precise motion modeling for each 3D Gaussian on a wider variety of objects.

MaGS introduces a relative deformation field MLP (RDF-MLP) that takes the encoded index of the mesh, the deformed mesh coordinates, and the relative Gaussian position on the mesh as input. By processing these inputs, the network computes and outputs Δ_α and Δ_μ , which are parameters that influence the final positions of the 3D Gaussians. These adjustments allow the Gaussians to hover dynamically on the deformed mesh rather than being fixed, thereby enhancing the adaptability and accuracy of the mesh deformation process, as shown in Figure 4.

The network’s optimization involves minimizing the difference between the predicted Gaussian positions and their actual positions on the mesh, ensuring that the non-rigid deformation field accurately reflects the true motion of the objects.

²We choose Poisson disk sampling for its ability to produce a highly uniform distribution of sample points. Other sampling methods are also applicable.

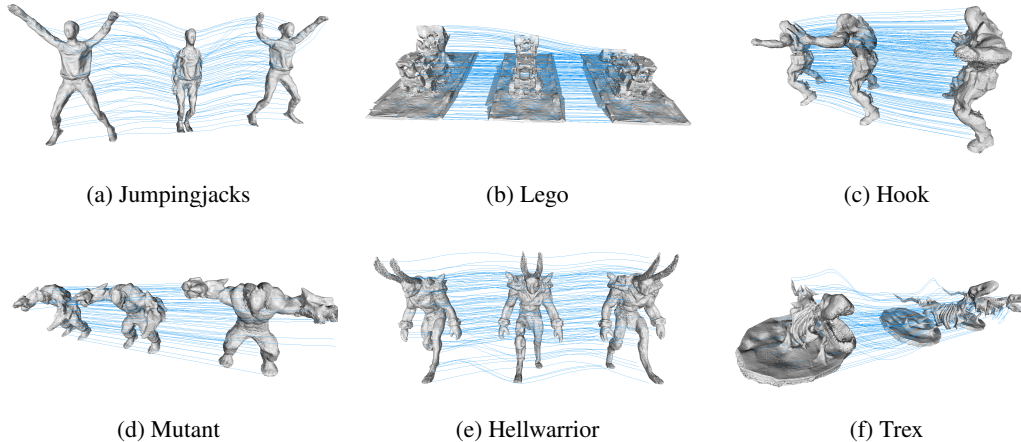


Figure 4: Illustration of mesh deformation and 3D Gaussians trajectories (indicated as blue lines) during MaGS deformation. As mesh deforms, Gaussians follow and hover on the facets flexibly.

4.2.4 3D Gaussian Splatting

Mesh-adsorbed Gaussians can be converted into standard 3D Gaussians as needed. This conversion is achieved by reconstructing a 3D Gaussians based on the parameters of the mesh-adsorbed Gaussians. For rendering, we use a differentiable renderer for splatting [15].

5 User-interactive Simulation

MaGS enables user-interactive simulations (*e.g.*, dragging) by directly modifying the mesh, which in turn updates the adsorbed 3D Gaussians for fast rendering. Initially, the ARAP algorithm is used to deform the mesh based on user-defined motions, minimizing distortion while preserving local rigidity, as defined by Eq. 10. The 3D Gaussians follow this deformation. Subsequently, the parameters of the deformed Mesh-adsorbed Gaussians are input into the RDF module to obtain a relative deformation field, which adjusts the positions of the 3D Gaussians with greater precision. Through these progressive deformations, MaGS maintains the fidelity of the object’s representation, enabling rational and flexible editing even for complex deformations.

6 Experiments

6.1 Experimental Settings

Implementation Details. We conducted experiments on D-NeRF and NeRF-DS datasets to evaluate and compare MaGS with previous methods. More details can be found in Appendix A.

Evaluation Metrics. The performance metrics used for evaluation include Peak Signal-to-Noise Ratio (PSNR), Structural Similarity Index (SSIM), Multi-Scale SSIM (MS-SSIM), and Learned Perceptual Image Patch Similarity (LPIPS)[53].

6.2 Quantitative Comparisons

For comparative evaluation, we benchmarked MaGS against state-of-the-art methods using the D-NeRF dataset at full resolution [33], as shown in Table 1, with additional results provided in the supplementary materials. Our method significantly outperformed the existing approaches. Specifically, compared to SC-GS, which exhibits the best reconstruction performance among other methods, MaGS achieves superior PSNR, SSIM, and LPIPS metrics across all seven³ tasks of the D-NeRF dataset. On average, MaGS improves the PSNR by 0.72 over SC-GS. More results on NeRF-DS can be found in Appendix B.

³Yang et al. [48] highlighted inconsistencies in the D-NeRF dataset’s Lego scene and offered a corrected version. Details on Lego-related experiments can be found in the appendix.



Figure 5: Qualitative comparison of dynamic view synthesis on the D-NeRF [33] dataset. We compare MaGS with D-NeRF [33], TiNeuVox-B [5], K-Planes [48], DeformableGS [48], 4D-GS [43], SC-GS [11]. Our method provides higher visual quality and preserves more details of dynamic scenes.

Table 1: Quantitative results on the synthesis dataset. The best, second-best, and third-best results are denoted by red, orange, and yellow. The rendering resolution is set to 800×800.

Type	Method	Jumpingjacks			Hellwarrior			Hook			Bouncingballs		
		PSNR↑	SSIM↑	LPIPS↓	PSNR↑	SSIM↑	LPIPS↓	PSNR↑	SSIM↑	LPIPS↓	PSNR↑	SSIM↑	LPIPS↓
Nerf Based	D-NeRF [33]	32.70	0.9779	0.0388	24.06	0.9440	0.0707	29.02	0.9595	0.0546	38.17	0.9891	0.0323
	TiNeuVox-B [5]	33.49	0.9771	0.0408	27.10	0.9638	0.0768	30.61	0.9599	0.0592	40.23	0.9926	0.0416
	Tensor4D [37]	24.20	0.9253	0.0667	31.26	0.9254	0.0735	28.63	0.9433	0.0636	24.47	0.9622	0.0437
	K-Planes [7]	31.11	0.9708	0.0468	24.58	0.9520	0.0824	28.12	0.9489	0.0662	40.05	0.9934	0.0322
GS Based	3D-GS [15]	20.64	0.9297	0.0828	29.89	0.9155	0.1056	21.71	0.8876	0.1034	23.20	0.9591	0.0600
	Deformable-GS [48]	37.72	0.9897	0.0126	41.54	0.9873	0.0234	37.42	0.9867	0.0144	41.01	0.9953	0.0093
	4D-GS [43]	35.42	0.9857	0.0128	28.71	0.9733	0.0369	32.73	0.9760	0.0272	40.62	0.9942	0.0155
	SC-GS [11]	40.06	0.9969	0.0106	42.33	0.9928	0.0266	39.20	0.9960	0.0134	42.11	0.9965	0.0213
Mesh-GS Based	DG-Mesh [18]	31.77	0.9770	0.0450	25.46	0.9590	0.0840	27.88	0.9540	0.0740	29.15	0.9690	0.0990
	Ours	42.02	0.9981	0.0077	42.63	0.9935	0.0249	39.80	0.9968	0.0111	42.42	0.9969	0.0176
Type	Method	Standup			Mutant			Trex			Average		
		PSNR↑	SSIM↑	LPIPS↓	PSNR↑	SSIM↑	LPIPS↓	PSNR↑	SSIM↑	LPIPS↓	PSNR↑	SSIM↑	LPIPS↓
Nerf Based	D-NeRF	33.13	0.9781	0.0355	30.31	0.9672	0.0392	30.61	0.9671	0.0535	31.14	0.9690	0.0464
	TiNeuVox-B	34.61	0.9797	0.0326	31.87	0.9607	0.0474	31.25	0.9666	0.0478	32.74	0.9715	0.0495
	Tensor4D	30.56	0.9581	0.0363	29.11	0.9451	0.0601	23.86	0.9351	0.0544	27.44	0.9421	0.0569
	K-Planes	33.10	0.9793	0.0310	32.50	0.9713	0.0362	30.43	0.9737	0.0343	31.41	0.9699	0.0470
GS Based	3D-GS	21.91	0.9301	0.0785	24.53	0.9336	0.0580	21.93	0.9539	0.0487	23.40	0.9299	0.0767
	Deformable-GS	44.62	0.9951	0.0063	42.63	0.9951	0.0052	38.10	0.9933	0.0098	40.43	0.9918	0.0116
	4D-GS	38.11	0.9898	0.0074	37.59	0.9880	0.0167	34.23	0.9850	0.0131	35.34	0.9846	0.0185
	SC-GS	46.72	0.9990	0.0068	43.54	0.9990	0.0067	40.17	0.9986	0.0119	42.02	0.9970	0.0139
Mesh-GS Based	DG-Mesh	30.21	0.9740	0.0510	30.40	0.9680	0.0550	28.95	0.9590	0.0650	29.12	0.9657	0.0676
	Ours	47.56	0.9992	0.0050	43.71	0.9991	0.0049	41.02	0.9988	0.0095	42.74	0.9975	0.0115

6.3 Qualitative Comparisons

Reconstruction. The comparisons on the D-NeRF dataset are shown in Figure 5, where magnified images highlight the details of the synthesized images. Our method produced results with superior visual quality. Additional comparisons are provided in the Appendix C.

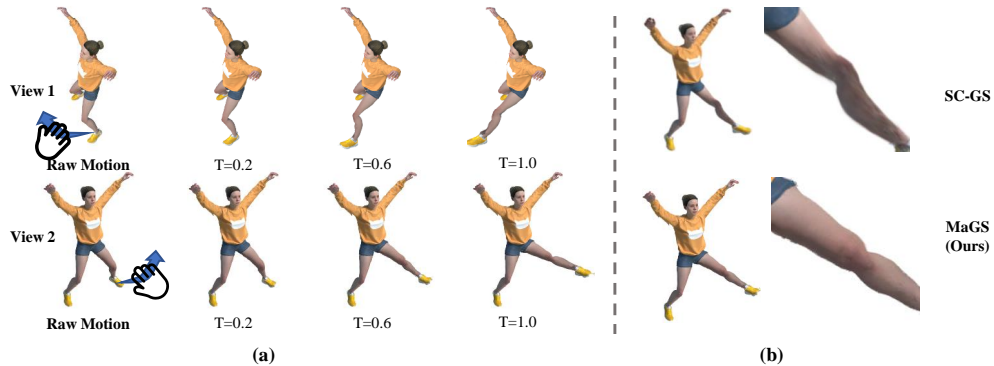


Figure 6: (a) Results of user-interactive editing on Mesh-adsorbed Gaussians using dragging. T denotes the intensity of the deformation. This motion is user-defined and not present in the dataset. MaGS preserves texture details and deformation rationality, maintaining high visual quality. (b) Rendering effect after deformation, compared with SC-GS [11].

Table 2: Ablation study on D-NeRF dataset using MaGS.

Method	Jumpingjacks			Hellwarrior			Hook			Bouncingballs		
	PSNR \uparrow	SSIM \uparrow	LPIPS \downarrow	PSNR \uparrow	SSIM \uparrow	LPIPS \downarrow	PSNR \uparrow	SSIM \uparrow	LPIPS \downarrow	PSNR \uparrow	SSIM \uparrow	LPIPS \downarrow
Ours w/o RDF	35.09	0.9928	0.0193	30.34	0.9853	0.0388	32.34	0.9874	0.0268	35.88	0.9917	0.0232
Ours w/o Hovering	40.42	0.9976	0.0085	42.24	0.9929	0.0279	36.56	0.9929	0.0229	41.08	0.9958	0.0236
Ours	42.02	0.9981	0.0077	42.63	0.9935	0.0249	39.80	0.9968	0.0111	42.42	0.9969	0.0176
Method	Standup			Mutant			Trex			Average		
	PSNR \uparrow	SSIM \uparrow	LPIPS \downarrow	PSNR \uparrow	SSIM \uparrow	LPIPS \downarrow	PSNR \uparrow	SSIM \uparrow	LPIPS \downarrow	PSNR \uparrow	SSIM \uparrow	LPIPS \downarrow
Ours w/o RDF	37.62	0.9960	0.0127	36.41	0.9940	0.0122	35.23	0.9939	0.0192	31.93	0.9776	0.0494
Ours w/o Hovering	47.11	0.9991	0.0054	43.60	0.9991	0.0049	39.88	0.9983	0.0045	37.75	0.9934	0.0176
Ours	47.56	0.9992	0.0050	43.71	0.9991	0.0049	41.02	0.9988	0.0095	41.80	0.9966	0.0146

Simulation. Figure 6 shows the new motions by simulating Jumpingjacks. As can be observed, our method can maintain the texture as much as possible after deformation, and the motion is more reasonable to maintain the object structure. Additional comparisons are provided in the Appendix C.

6.4 Ablation Studies

We ablate MaGS to understand the contribution of the two key design decisions with the default settings, including Mesh-adsorbed 3D Gaussians representation, and non-rigid deformation field. To ablate the Mesh-adsorbed 3D Gaussians representation, we disable the “hovering” attribute, converting the *mesh-adsorbed* pattern to a *mesh-anchored* one. As shown in Table 2, this ablation slightly decreases rendering performance. On the D-NeRF dataset, the PSNR drops range from 0.11 (mutant) to 3.24 (hook), with an average PSNR decrease of 1.18 (2.8%) across all seven items.

To ablate the relative deformation field, we simulate the dynamic target based on the ARAP prior of the vanilla mesh merely. As shown in Table 2, this change significantly decreases rendering performance. On the D-NeRF dataset, the PSNR drops range from 5.79 (Trex) to 12.29 (Hellwarrior), with an average PSNR decrease of 8.04 (18%) across all seven items.

7 Conclusion and Future Works

This paper introduces the MaGS method, which addresses 3D reconstruction and simulation by constraining 3D Gaussians to hover on the mesh surface. This approach maintains structural integrity and achieves high rendering accuracy for dynamic objects. The learnable RDF enhances traditional mesh-driven deformation by precisely modeling the relative displacement between the mesh and 3D Gaussians. Extensive experiments on the D-NeRF and NeRF-DS datasets show that MaGS outperforms current methods in reconstruction and simulation, reducing floating points and artifacts. This demonstrates MaGS’s potential to advance 3D reconstruction and simulation, with future research needed to refine its capabilities and applications. We further illustrate our limitations and social impacts in Appendix D and E.

References

- [1] Åke Björck. Numerics of gram-schmidt orthogonalization. *Linear Algebra and Its Applications*, 197: 297–316, 1994. ISBN: 0024-3795 Publisher: Elsevier. 6
- [2] Ang Cao and Justin Johnson. HexPlane: A Fast Representation for Dynamic Scenes. *CoRR*, abs/2301.09632, 2023. doi: 10.48550/ARXIV.2301.09632. URL <https://doi.org/10.48550/arXiv.2301.09632>. 3
- [3] Guikun Chen and Wenguan Wang. A Survey on 3D Gaussian Splatting. *CoRR*, abs/2401.03890, 2024. doi: 10.48550/ARXIV.2401.03890. URL <https://doi.org/10.48550/arXiv.2401.03890>. 2
- [4] Yufan Chen, Lizhen Wang, Qijing Li, Hongjiang Xiao, Shengping Zhang, Hongxun Yao, and Yebin Liu. MonoGaussianAvatar: Monocular Gaussian Point-based Head Avatar. *CoRR*, abs/2312.04558, 2023. doi: 10.48550/ARXIV.2312.04558. URL <https://doi.org/10.48550/arXiv.2312.04558>. 3
- [5] Jiemin Fang, Taoran Yi, Xinggang Wang, Lingxi Xie, Xiaopeng Zhang, Wenyu Liu, Matthias Nießner, and Qi Tian. Fast Dynamic Radiance Fields with Time-aware Neural Voxels. *CoRR*, abs/2205.15285, 2022. doi: 10.48550/ARXIV.2205.15285. URL <https://doi.org/10.48550/arXiv.2205.15285>. 3, 8, 16, 17
- [6] Yutao Feng, Xiang Feng, Yintong Shang, Ying Jiang, Chang Yu, Zeshun Zong, Tianjia Shao, Hongzhi Wu, Kun Zhou, Chenfanfu Jiang, and Yin Yang. Gaussian Splashing: Dynamic Fluid Synthesis with Gaussian Splatting. *CoRR*, abs/2401.15318, 2024. doi: 10.48550/ARXIV.2401.15318. URL <https://doi.org/10.48550/arXiv.2401.15318>. 2
- [7] Sara Fridovich-Keil, Giacomo Meanti, Frederik Warburg, Benjamin Recht, and Angjoo Kanazawa. K-Planes: Explicit Radiance Fields in Space, Time, and Appearance. *CoRR*, abs/2301.10241, 2023. doi: 10.48550/ARXIV.2301.10241. URL <https://doi.org/10.48550/arXiv.2301.10241>. 2, 3, 8
- [8] Chen Gao, Ayush Saraf, Johannes Kopf, and Jia-Bin Huang. Dynamic View Synthesis from Dynamic Monocular Video. *CoRR*, abs/2105.06468, 2021. URL <https://arxiv.org/abs/2105.06468>. 2
- [9] Antoine Guédon and Vincent Lepetit. SuGaR: Surface-aligned Gaussian Splatting for Efficient 3D Mesh Reconstruction and High-quality Mesh Rendering. *CoRR*, abs/2311.12775, 2023. doi: 10.48550/ARXIV.2311.12775. URL <https://doi.org/10.48550/arXiv.2311.12775>. 2, 3, 4, 5
- [10] Wenbo Hu, Yuling Wang, Lin Ma, Bangbang Yang, Lin Gao, Xiao Liu, and Yuewen Ma. Tri-MipRF: Tri-mip Representation for Efficient Anti-aliasing Neural Radiance Fields. *CoRR*, abs/2307.11335, 2023. doi: 10.48550/ARXIV.2307.11335. URL <https://doi.org/10.48550/arXiv.2307.11335>. 2, 3
- [11] Yi-Hua Huang, Yang-Tian Sun, Ziyi Yang, Xiaoyang Lyu, Yan-Pei Cao, and Xiaojuan Qi. SC-GS: Sparse-controlled Gaussian Splatting for Editable Dynamic Scenes. *CoRR*, abs/2312.14937, 2023. doi: 10.48550/ARXIV.2312.14937. URL <https://doi.org/10.48550/arXiv.2312.14937>. 2, 3, 8, 9, 16, 17
- [12] Wei Jiang, Kwang Moo Yi, Golnoosh Samei, Oncel Tuzel, and Anurag Ranjan. NeuMan: Neural Human Radiance Field from a Single Video. *CoRR*, abs/2203.12575, 2022. doi: 10.48550/ARXIV.2203.12575. URL <https://doi.org/10.48550/arXiv.2203.12575>. 2
- [13] Ying Jiang, Chang Yu, Tianyi Xie, Xuan Li, Yutao Feng, Huamin Wang, Minchen Li, Henry Y. K. Lau, Feng Gao, Yin Yang, and Chenfanfu Jiang. VR-GS: A Physical Dynamics-aware Interactive Gaussian Splatting System in Virtual Reality. *CoRR*, abs/2401.16663, 2024. doi: 10.48550/ARXIV.2401.16663. URL <https://doi.org/10.48550/arXiv.2401.16663>. 2
- [14] HyunJun Jung, Nikolas Brasch, Jifei Song, Eduardo Pérez-Pellitero, Yiren Zhou, Zhihao Li, Nassir Navab, and Benjamin Busam. Deformable 3D Gaussian Splatting for Animatable Human Avatars. *CoRR*, abs/2312.15059, 2023. doi: 10.48550/ARXIV.2312.15059. URL <https://doi.org/10.48550/arXiv.2312.15059>. 3
- [15] Bernhard Kerbl, Georgios Kopanas, Thomas Leimkühler, and George Drettakis. 3D Gaussian Splatting for Real-time Radiance Field Rendering. *CoRR*, abs/2308.04079, 2023. doi: 10.48550/ARXIV.2308.04079. URL <https://doi.org/10.48550/arXiv.2308.04079>. 2, 3, 7, 8
- [16] Diederik P. Kingma and Jimmy Ba. Adam: A Method for Stochastic Optimization. In Yoshua Bengio and Yann LeCun, editors, *3rd International Conference on Learning Representations, ICLR 2015, San Diego, CA, USA, May 7-9, 2015, Conference Track Proceedings*, 2015. URL <http://arxiv.org/abs/1412.6980>. 14

- [17] Christoph Lassner and Michael Zollhöfer. Pulsar: Efficient Sphere-based Neural Rendering. In *IEEE Conference on Computer Vision and Pattern Recognition, CVPR 2021, virtual, June 19-25, 2021*, pages 1440–1449. Computer Vision Foundation / IEEE, 2021. doi: 10.1109/CVPR46437.2021.00149. URL https://openaccess.thecvf.com/content/CVPR2021/html/Lassner_Pulsar_Efficient_Sphere-Based_Neural_Rendering_CVPR_2021_paper.html. 2
- [18] Isabella Liu, Hao Su, and Xiaolong Wang. Dynamic gaussians mesh: consistent mesh reconstruction from monocular videos, April 2024. URL <http://arxiv.org/abs/2404.12379>. arXiv:2404.12379 [cs]. 2, 3, 5, 8, 15, 16
- [19] Jiawei Liu, Yan-Pei Cao, Weijia Mao, Wenqiao Zhang, David Junhao Zhang, Jussi Keppo, Ying Shan, Xiaohu Qie, and Mike Zheng Shou. DeVRF: Fast Deformable Voxel Radiance Fields for Dynamic Scenes. *CoRR*, abs/2205.15723, 2022. doi: 10.48550/ARXIV.2205.15723. URL <https://doi.org/10.48550/arXiv.2205.15723>. 3
- [20] Matthew Loper, Naureen Mahmood, Javier Romero, Gerard Pons-Moll, and Michael J. Black. SMPL: a skinned multi-person linear model. *ACM Trans. Graph.*, 34(6):248:1–248:16, 2015. doi: 10.1145/2816795.2818013. URL <https://doi.org/10.1145/2816795.2818013>. 2
- [21] William E. Lorensen and Harvey E. Cline. Marching cubes: A high resolution 3D surface construction algorithm. In Maureen C. Stone, editor, *Proceedings of the 14th Annual Conference on Computer Graphics and Interactive Techniques, SIGGRAPH 1987, Anaheim, California, USA, July 27-31, 1987*, pages 163–169. ACM, 1987. doi: 10.1145/37401.37422. URL <https://doi.org/10.1145/37401.37422>. 4
- [22] Keyang Luo, Tao Guan, Lili Ju, Haipeng Huang, and Yawei Luo. P-MVSNet: Learning Patch-wise Matching Confidence Aggregation for Multi-view Stereo. In *2019 IEEE/CVF International Conference on Computer Vision, ICCV 2019, Seoul, Korea (South), October 27 - November 2, 2019*, pages 10451–10460. IEEE, 2019. doi: 10.1109/ICCV.2019.01055. URL <https://doi.org/10.1109/ICCV.2019.01055>. 2
- [23] Keyang Luo, Tao Guan, Lili Ju, Yuesong Wang, Zhuo Chen, and Yawei Luo. Attention-aware Multi-view Stereo. In *2020 IEEE/CVF Conference on Computer Vision and Pattern Recognition, CVPR 2020, Seattle, WA, USA, June 13-19, 2020*, pages 1587–1596. Computer Vision Foundation / IEEE, 2020. doi: 10.1109/CVPR42600.2020.00166. URL https://openaccess.thecvf.com/content_CVPR_2020/html/Luo_Attention-Aware_Multi-View_Stereo_CVPR_2020_paper.html. 2
- [24] Jiarui Meng, Haijie Li, Yanmin Wu, Qiankun Gao, Shuzhou Yang, Jian Zhang, and Siwei Ma. Mirror-3DGS: Incorporating Mirror Reflections into 3D Gaussian Splatting. *CoRR*, abs/2404.01168, 2024. doi: 10.48550/ARXIV.2404.01168. URL <https://doi.org/10.48550/arXiv.2404.01168>. 2
- [25] Qiaowei Miao, Yawei Luo, and Yi Yang. PLA4D: Pixel-level Alignments for Text-to-4D Gaussian Splatting. *CoRR*, abs/2405.19957, 2024. URL <https://arxiv.org/abs/2405.19957>. 2
- [26] Ben Mildenhall, Pratul P. Srinivasan, Matthew Tancik, Jonathan T. Barron, Ravi Ramamoorthi, and Ren Ng. NeRF: Representing Scenes as Neural Radiance Fields for View Synthesis. *CoRR*, abs/2003.08934, 2020. URL <https://arxiv.org/abs/2003.08934>. 2
- [27] Zhiyuan Min, Yawei Luo, Wei Yang, Yuesong Wang, and Yi Yang. Entangled View-epipolar Information Aggregation for Generalizable Neural Radiance Fields. *CoRR*, abs/2311.11845, 2023. doi: 10.48550/ARXIV.2311.11845. URL <https://doi.org/10.48550/arXiv.2311.11845>. 2
- [28] Arthur Moreau, Jifei Song, Helisa Dhama, Richard Shaw, Yiren Zhou, and Eduardo Pérez-Pellitero. Human Gaussian Splatting: Real-time Rendering of Animatable Avatars. *CoRR*, abs/2311.17113, 2023. doi: 10.48550/ARXIV.2311.17113. URL <https://doi.org/10.48550/arXiv.2311.17113>. 3
- [29] Thomas Müller, Alex Evans, Christoph Schied, and Alexander Keller. Instant Neural Graphics Primitives with a Multiresolution Hash Encoding. *CoRR*, abs/2201.05989, 2022. URL <https://arxiv.org/abs/2201.05989>. 2
- [30] Keunhong Park, Utkarsh Sinha, Jonathan T. Barron, Sofien Bouaziz, Dan B. Goldman, Steven M. Seitz, and Ricardo Martin-Brualla. Nerfies: Deformable Neural Radiance Fields. In *2021 IEEE/CVF International Conference on Computer Vision, ICCV 2021, Montreal, QC, Canada, October 10-17, 2021*, pages 5845–5854. IEEE, 2021. doi: 10.1109/ICCV48922.2021.00581. URL <https://doi.org/10.1109/ICCV48922.2021.00581>. 3
- [31] Keunhong Park, Utkarsh Sinha, Peter Hedman, Jonathan T. Barron, Sofien Bouaziz, Dan B. Goldman, Ricardo Martin-Brualla, and Steven M. Seitz. HyperNeRF: A Higher-dimensional Representation for Topologically Varying Neural Radiance Fields. *CoRR*, abs/2106.13228, 2021. URL <https://arxiv.org/abs/2106.13228>. 3

- [32] Adam Paszke, Sam Gross, Soumith Chintala, Gregory Chanan, Edward Yang, Zachary DeVito, Zeming Lin, Alban Desmaison, Luca Antiga, and Adam Lerer. Automatic differentiation in PyTorch. In *NeurIPS*, 2017. 14
- [33] Albert Pumarola, Enric Corona, Gerard Pons-Moll, and Francesc Moreno-Noguer. D-NeRF: Neural Radiance Fields for Dynamic Scenes. *CoRR*, abs/2011.13961, 2020. URL <https://arxiv.org/abs/2011.13961>. 2, 3, 7, 8, 14, 15, 16, 17
- [34] Zhiyin Qian, Shaofei Wang, Marko Mihajlovic, Andreas Geiger, and Siyu Tang. 3DGS-Avatar: Animatable Avatars via Deformable 3D Gaussian Splatting. *CoRR*, abs/2312.09228, 2023. doi: 10.48550/ARXIV.2312.09228. URL <https://doi.org/10.48550/arXiv.2312.09228>. 3
- [35] Yi-Ling Qiao, Alexander Gao, Yiran Xu, Yue Feng, Jia-Bin Huang, and Ming C. Lin. Dynamic Mesh-aware Radiance Fields. *CoRR*, abs/2309.04581, 2023. doi: 10.48550/ARXIV.2309.04581. URL <https://doi.org/10.48550/arXiv.2309.04581>. 2
- [36] Johannes L. Schönberger and Jan-Michael Frahm. Structure-from-motion Revisited. In *2016 IEEE Conference on Computer Vision and Pattern Recognition, CVPR 2016, Las Vegas, NV, USA, June 27-30, 2016*, pages 4104–4113. IEEE Computer Society, 2016. doi: 10.1109/CVPR.2016.445. URL <https://doi.org/10.1109/CVPR.2016.445>. 14
- [37] Ruizhi Shao, Zerong Zheng, Hanzhang Tu, Boning Liu, Hongwen Zhang, and Yebin Liu. Tensor4D : Efficient Neural 4D Decomposition for High-fidelity Dynamic Reconstruction and Rendering. *CoRR*, abs/2211.11610, 2022. doi: 10.48550/ARXIV.2211.11610. URL <https://doi.org/10.48550/arXiv.2211.11610>. 3, 8
- [38] Olga Sorkine and Marc Alexa. As-rigid-as-possible surface modeling. In Alexander G. Belyaev and Michael Garland, editors, *Proceedings of the Fifth Eurographics Symposium on Geometry Processing, Barcelona, Spain, July 4-6, 2007*, volume 257 of *ACM International Conference Proceeding Series*, pages 109–116. Eurographics Association, 2007. doi: 10.2312/SGP/SGP07/109-116. URL <https://doi.org/10.2312/SGP/SGP07/109-116>. 2, 3
- [39] Edgar Tretschk, Ayush Tewari, Vladislav Golyanik, Michael Zollhöfer, Christoph Lassner, and Christian Theobalt. Non-rigid Neural Radiance Fields: Reconstruction and Novel View Synthesis of a Dynamic Scene From Monocular Video. In *2021 IEEE/CVF International Conference on Computer Vision, ICCV 2021, Montreal, QC, Canada, October 10-17, 2021*, pages 12939–12950. IEEE, 2021. doi: 10.1109/ICCV48922.2021.01272. URL <https://doi.org/10.1109/ICCV48922.2021.01272>. 3
- [40] Joanna Waczynska, Piotr Borycki, Sławomir Konrad Tadeja, Jacek Tabor, and Przemysław Spurek. GaMeS: Mesh-based Adapting and Modification of Gaussian Splatting. *CoRR*, abs/2402.01459, 2024. doi: 10.48550/ARXIV.2402.01459. URL <https://doi.org/10.48550/arXiv.2402.01459>. 2, 3, 5
- [41] Yuesong Wang, Tao Guan, Zhuo Chen, Yawei Luo, Keyang Luo, and Lili Ju. Mesh-guided Multi-view Stereo With Pyramid Architecture. In *2020 IEEE/CVF Conference on Computer Vision and Pattern Recognition, CVPR 2020, Seattle, WA, USA, June 13-19, 2020*, pages 2036–2045. Computer Vision Foundation / IEEE, 2020. doi: 10.1109/CVPR42600.2020.00211. URL https://openaccess.thecvf.com/content_CVPR_2020/html/Wang_Mesh-Guided_Multi-View_Stereo_With_Pyramid_Architecture_CVPR_2020_paper.html. 2
- [42] Yuesong Wang, Zhaojie Zeng, Tao Guan, Wei Yang, Zhuo Chen, Wenkai Liu, Luoyuan Xu, and Yawei Luo. Adaptive Patch Deformation for Textureless-resilient Multi-view Stereo. In *IEEE/CVF Conference on Computer Vision and Pattern Recognition, CVPR 2023, Vancouver, BC, Canada, June 17-24, 2023*, pages 1621–1630. IEEE, 2023. doi: 10.1109/CVPR52729.2023.00162. URL <https://doi.org/10.1109/CVPR52729.2023.00162>. 2
- [43] Guanjun Wu, Taoran Yi, Jiemin Fang, Lingxi Xie, Xiaopeng Zhang, Wei Wei, Wenyu Liu, Qi Tian, and Xinggang Wang. 4D Gaussian Splatting for Real-time Dynamic Scene Rendering. *CoRR*, abs/2310.08528, 2023. doi: 10.48550/ARXIV.2310.08528. URL <https://doi.org/10.48550/arXiv.2310.08528>. 2, 3, 8, 16, 17
- [44] Tianyi Xie, Zeshun Zong, Yuxing Qiu, Xuan Li, Yutao Feng, Yin Yang, and Chenfanfu Jiang. PhysGaussian: Physics-integrated 3D Gaussians for Generative Dynamics. *CoRR*, abs/2311.12198, 2023. doi: 10.48550/ARXIV.2311.12198. URL <https://doi.org/10.48550/arXiv.2311.12198>. 2
- [45] Zhiwen Yan, Chen Li, and Gim Hee Lee. NeRF-DS: Neural Radiance Fields for Dynamic Specular Objects. *CoRR*, abs/2303.14435, 2023. doi: 10.48550/ARXIV.2303.14435. URL <https://doi.org/10.48550/arXiv.2303.14435>. 3, 15, 17

- [46] Bangbang Yang, Chong Bao, Junyi Zeng, Hujun Bao, Yinda Zhang, Zhaopeng Cui, and Guofeng Zhang. NeuMesh: Learning Disentangled Neural Mesh-based Implicit Field for Geometry and Texture Editing. *CoRR*, abs/2207.11911, 2022. doi: 10.48550/ARXIV.2207.11911. URL <https://doi.org/10.48550/arXiv.2207.11911>. 2, 3
- [47] Zeyu Yang, Hongye Yang, Zijie Pan, Xiatian Zhu, and Li Zhang. Real-time Photorealistic Dynamic Scene Representation and Rendering with 4D Gaussian Splatting. *CoRR*, abs/2310.10642, 2023. doi: 10.48550/ARXIV.2310.10642. URL <https://doi.org/10.48550/arXiv.2310.10642>. 2
- [48] Ziyi Yang, Xinyu Gao, Wen Zhou, Shaohui Jiao, Yuqing Zhang, and Xiaogang Jin. Deformable 3D Gaussians for High-fidelity Monocular Dynamic Scene Reconstruction. *CoRR*, abs/2309.13101, 2023. doi: 10.48550/ARXIV.2309.13101. URL <https://doi.org/10.48550/arXiv.2309.13101>. 2, 3, 7, 8, 16, 17
- [49] Ye Yuan, Shih-En Wei, Tomas Simon, Kris Kitani, and Jason M. Saragih. SimPoE: Simulated Character Control for 3D Human Pose Estimation. *CoRR*, abs/2104.00683, 2021. URL <https://arxiv.org/abs/2104.00683>. 2
- [50] Yu-Jie Yuan, Yang-Tian Sun, Yu-Kun Lai, Yuewen Ma, Rongfei Jia, and Lin Gao. NeRF-Editing: Geometry Editing of Neural Radiance Fields. *CoRR*, abs/2205.04978, 2022. doi: 10.48550/ARXIV.2205.04978. URL <https://doi.org/10.48550/arXiv.2205.04978>. 2, 3
- [51] Cem Yuksel. Sample Elimination for Generating Poisson Disk Sample Sets. *Comput. Graph. Forum*, 34(2):25–32, 2015. doi: 10.1111/CGF.12538. URL <https://doi.org/10.1111/cgf.12538>. 6
- [52] Qiang Zhang, Seung-Hwan Baek, Szymon Rusinkiewicz, and Felix Heide. Differentiable Point-based Radiance Fields for Efficient View Synthesis. *CoRR*, abs/2205.14330, 2022. doi: 10.48550/ARXIV.2205.14330. URL <https://doi.org/10.48550/arXiv.2205.14330>. 2
- [53] Richard Zhang, Phillip Isola, Alexei A. Efros, Eli Shechtman, and Oliver Wang. The Unreasonable Effectiveness of Deep Features as a Perceptual Metric. *CoRR*, abs/1801.03924, 2018. URL <http://arxiv.org/abs/1801.03924>. 7
- [54] Licheng Zhong, Hong-Xing Yu, Jiajun Wu, and Yunzhu Li. Reconstruction and Simulation of Elastic Objects with Spring-mass 3D Gaussians. *CoRR*, abs/2403.09434, 2024. doi: 10.48550/ARXIV.2403.09434. URL <https://doi.org/10.48550/arXiv.2403.09434>. 2

A Datasets and Implementation Details

We conducted experiments on D-NeRF and NeRF-DS datasets to evaluate and compare MaGS with previous state-of-the-art methods. The D-NeRF dataset comprises eight dynamic scenes with precise camera parameter information. For the D-NeRF dataset, we tested our method at both full resolution (800*800) and half resolution (400*400). The NeRF-DS dataset comprises seven videos captured with camera poses estimated using COLMAP. We benchmark MaGS on NeRF-DS at its original resolution (480*270).

We use PyTorch [32] for our implementation. The training process is composed of two stages.

In Stage I, we train the 3D Gaussians and the DF-MLP to obtain a coarse representation of the dynamic object. The optimization process in Stage I begins with initializing 3D Gaussians with COLMAP SfM points [36] or random points. During the initial iterations, we do not employ the deformation field, allowing the Gaussian point cloud to quickly acquire a rough representation of the object as a warming-up step. Once it converges, we joint optimize both the 3D Gaussians and the DF-MLP. We employ an 8-layer fully connected network as the backbone and add skip connections in the fourth layer. We use Adam [16] as the optimizer, with a weight decay of $5e-4$. We train the network for a total of $30k$ iterations, with the first 600 as the warm-up stage during which the learning rate increases linearly from 0 to the initial value. Then the learning rate is divided by ten at 10k and 20k iterations. In our best model, we set hyper-parameters $\lambda = 2e - 4$, $\lambda_s = 1.0$, $\lambda_k = 1.0$, $\lambda_r = 5.0$, respectively. We use a combination of L1 loss and D-SSIM loss to optimize the deformation network and 3D Gaussian, the rate of D-SSIM is 0.2.

In Stage II, we train the Mesh-adsorbed Gaussians and Relative Deformation Fields MLP (RDF-MLP) to obtain a finer 3D dynamic representation that satisfies both reconstruction and simulation tasks. It should be noted that the mesh deformation based on DF-MLP and ARAP only provides MaGS deformation information and does not require optimization. The parameters to be learned include the coordinates of the vertices of the mesh, the parameters of the 3D Gaussians, the α parameters that control the positions of the 3D Gaussians on the mesh, and the Relative Deformation Field (in form of the weights within RDF-MLP). All these parameters are optimized simultaneously. We use a combination of L1 loss and D-SSIM loss to optimize the deformation network and 3D Gaussian, the rate of D-SSIM is 0.2.

To facilitate the reproduction of our results, we elaborated all our hyperparameters in Table 3.

Table 3: Hyper Parameters

var	value	
position_lr_init	0.00016	Settings of 3DGS
position_lr_final	1.6E-06	Settings of 3DGS
position_lr_delay_mult	0.01	Settings of 3DGS
position_lr_max_steps	80_000	Settings of 3DGS
deform_lr_max_steps	80_000	Settings of 3DGS
feature_lr	0.0025	Settings of 3DGS
opacity_lr	0.05	Settings of 3DGS
scaling_lr	0.001	Settings of 3DGS
rotation_lr	0.001	Settings of 3DGS
percent_dense	0.01	Settings of 3DGS
lambda_dssim	0.2	Settings of 3DGS
densification_interval	100	Settings of 3DGS
opacity_reset_interval	3000	Settings of 3DGS
densify_from_iter	500	Settings of 3DGS
densify_until_iter	50_000	Settings of 3DGS
densify_grad_threshold	0.0002	Settings of 3DGS
oneupSHdegree_step	1000	Settings of 3DGS
random_bg_color	FALSE	Settings of 3DGS
deform_lr_scale	1	deform_lr = position_lr_init * deform_lr_scale
iterations	40_000	for stage1 and stage 2
warm_up	3_000	for stage1
vertices_lr	0.00016	for stage2, mesh refine
alpha_lr	0.0001	for stage2

B Additional Quantitative Results

For comparative evaluation, we benchmarked MaGS against state-of-the-art methods using the D-NeRF dataset at half resolution [33], as shown in Table 4, as additional evaluations. Our method significantly outperformed the existing approaches. Specifically, compared to SC-GS, which exhibits the best reconstruction performance among other methods, MaGS achieves superior PSNR, SSIM, and LPIPS metrics across 6 tasks of the D-NeRF dataset except the Bouncingballs. Due to the

Table 4: Quantitative results on the synthesis dataset. The best, second-best, and third-best results are denoted by **red**, **orange**, and **yellow**. The rendering resolution is set to 400×400.

Type	Method	Bouncingballs			Hellwarrior			Hook			Jumpingjacks		
		PSNR↑	SSIM↑	LPIPS↓	PSNR↑	SSIM↑	LPIPS↓	PSNR↑	SSIM↑	LPIPS↓	PSNR↑	SSIM↑	LPIPS↓
Nerf Based	D-NeRF	38.37	0.9892	0.0194	28.46	0.9242	0.0778	30.44	0.9712	0.0496	33.77	0.9854	0.0284
	TiNeuVox-B	40.91	0.9944	0.0162	30.68	0.9354	0.0725	32.48	0.9804	0.0503	35.56	0.9898	0.0263
	Tensor4D	25.36	0.9610	0.0411	31.40	0.9250	0.0675	29.03	0.9550	0.4990	24.01	0.9190	0.0768
	K-Planes	40.61	0.9910	0.2970	25.27	0.9480	0.0755	28.59	0.9530	0.5810	32.27	0.9710	0.0389
	D-GS	36.91	0.9952	0.0118	41.18	0.9890	0.0227	36.44	0.9927	0.0158	37.90	0.9956	0.0096
	4D-GS	40.97	0.9946	0.0122	31.85	0.9475	0.0578	33.94	0.9850	0.0260	36.74	0.9928	0.0151
Mesh-GS Based	SCGS	44.91	0.9980	0.0166	42.93	0.9940	0.0155	39.89	0.9970	0.0076	41.13	0.9980	0.0067
	MaGS (Ours)	42.32	0.9969	0.0110	43.56	0.9942	0.0143	40.14	0.9970	0.0072	43.22	0.9985	0.0038
Type	Method	Mutant			Standup			Trex			Average		
		PSNR↑	SSIM↑	LPIPS↓	PSNR↑	SSIM↑	LPIPS↓	PSNR↑	SSIM↑	LPIPS↓	PSNR↑	SSIM↑	LPIPS↓
Nerf Based	D-NeRF	32.34	0.9791	0.0312	34.45	0.9819	0.0244	32.14	0.9863	0.0210	32.85	0.9739	0.0360
	TiNeuVox-B	33.80	0.9845	0.0360	36.00	0.9865	0.0238	33.27	0.9918	0.0213	34.67	0.9804	0.0352
	Tensor4D	29.99	0.9510	0.0422	30.86	0.9640	0.0214	23.51	0.9340	0.0640	27.74	0.9441	0.1160
	K-Planes	33.79	0.9820	0.0207	34.31	0.9840	0.0194	31.41	0.9800	0.0234	32.32	0.9727	0.1508
	D-GS	40.86	0.9979	0.0050	41.90	0.9976	0.0053	35.88	0.9957	0.0072	38.72	0.9948	0.0111
	4D-GS	37.28	0.9926	0.0142	37.88	0.9918	0.0135	35.15	0.9945	0.0113	36.26	0.9856	0.0215
Mesh-GS Based	SCGS	45.19	0.9990	0.0028	47.89	0.9990	0.0023	41.24	0.9980	0.0046	43.31	0.9976	0.0080
	MaGS (Ours)	45.40	0.9992	0.0024	48.33	0.9994	0.0018	41.20	0.9989	0.0033	43.45	0.9977	0.0062

Table 5: Quantitative results on the NeRF-DS dataset. The dataset was captured using a fixed camera view, in which MaGS can not obtain an accurate initial mesh for 3D Gaussians. In such scenarios, MaGS can only produce results comparable to existing methods rather than surpassing them.

Methods	Bell			Sheet			Press			Basin		
	PSNR↑	MS-SSIM↑	LPIPS↓	PSNR↑	MS-SSIM↑	LPIPS↓	PSNR↑	MS-SSIM↑	LPIPS↓	PSNR↑	MS-SSIM↑	LPIPS↓
HyperNeRF	24.00	0.8840	0.1590	24.30	0.8740	0.1480	25.40	0.8730	0.1640	20.20	0.8290	0.1680
NeRF-DS	23.30	0.8720	0.1340	25.70	0.9180	0.1150	26.40	0.9110	0.1230	20.30	0.8680	0.1270
TiNeuVox-B	23.10	0.8760	0.1130	21.10	0.7450	0.2340	24.10	0.8920	0.1330	20.70	0.8960	0.1050
SC-GS	25.10	0.9180	0.1170	26.20	0.8980	0.1420	26.60	0.9010	0.1350	19.60	0.8460	0.1540
Ours	25.21	0.8337	0.1198	22.93	0.7927	0.2552	25.81	0.9021	0.1338	19.01	0.7561	0.1593
Methods	Cup			Sieve			Plate			Average		
	PSNR↑	MS-SSIM↑	LPIPS↓	PSNR↑	MS-SSIM↑	LPIPS↓	PSNR↑	MS-SSIM↑	LPIPS↓	PSNR↑	MS-SSIM↑	LPIPS↓
HyperNeRF	20.50	0.7050	0.3180	25.00	0.9090	0.1290	18.10	0.7140	0.3590	22.50	0.8269	0.2064
NeRF-DS	24.50	0.9160	0.1180	26.10	0.9350	0.1080	20.80	0.8670	0.1640	23.87	0.8981	0.1270
TiNeuVox-B	20.50	0.8060	0.1820	20.10	0.8220	0.2050	20.60	0.8630	0.1610	21.46	0.8429	0.1619
SC-GS	24.50	0.9160	0.1150	26.00	0.9190	0.1140	20.20	0.8370	0.2020	24.03	0.8907	0.1399
Ours	24.23	0.9049	0.1441	26.53	0.9165	0.1092	18.26	0.7456	0.2801	23.14	0.8360	0.1716

low-resolution and tiny-volume characteristic of the bouncing ball object, the initial mesh is cracked, influencing the following MaGS. On average, MaGS improves the PSNR by 0.14 over SC-GS and significantly outperforms other methods. We conducted an evaluation in a full-resolution lego scene, as shown in Table 6, and compared our method with the SC-GS and D-GS (Deformable-GS). MaGS improves the PSNR by greater than 1.

For comparative evaluation, we benchmarked MaGS against state-of-the-art methods using the NeRF-DS dataset at full resolution [45], as shown in Table 5, as additional evaluations. Our method achieved the best performance on the Sieve metric, surpassing SC-GS by 0.6 in PSNR. In terms of average metric, our method did not show a significant difference compared to other methods. The optimal metric provided by SC-GS was only 4% higher than our method.

C Additional Qualitative Results

In the qualitative comparison of dynamic view synthesis on the D-NeRF [33] dataset, we compare our method with the DG-Mesh [18] approach. To the best of our knowledge, DG-Mesh is the most related method to ours. Nevertheless, it employs a fixed and anchored mesh-Gaussian relation, which faces a trade-off between simulation and reconstruction according to our analysis. The comparisons are shown in Figure 7. As can be seen, due to the fixed one-to-one relation, the mesh can not be well-matched to the video. Our method demonstrates superior performance in both mesh reconstruction accuracy and rendering precision, preserving more intricate details.

Table 6: Quantitative results on lego. The best results are denoted by **red**. The rendering resolution is set to 800×800.

Method	Lego (D-NeRF version)			Lego (D-GS version)		
	PSNR↑	SSIM↑	LPIPS↓	PSNR↑	SSIM↑	LPIPS↓
D-GS	24.86	0.9417	0.0447	33.07	0.9794	0.0183
SCGS	22.59	0.9100	0.0641	33.11	0.9886	0.0178
Ours	25.44	0.9500	0.0377	34.66	0.9921	0.0117



Figure 7: Qualitative comparison between DG-Mesh [18] and MaGS.

In addition, we give more qualitative results from MaGS on Mutant and Standup, compared with D-NeRF [33], TiNeuVox-B [5], K-Planes [48], DeformableGS [48], 4D-GS [43], SC-GS [11]. Our method provides higher visual quality and preserves more details of dynamic scenes.

D Limitations

Our method depends significantly on an accurate initial mesh. Consequently, it faces challenges in low-resolution images and scenes with limited viewing angles. For instance, NeRF-DS is a dataset with a fixed viewing angle. In such scenarios, MaGS can only produce results comparable to existing methods rather than surpassing them. Therefore, our approach is more suited to scenes with comprehensive viewing angles and high resolution.

As shown in Figure 9 and Figure 10, in several examples where MaGS performed poorly, incomplete meshes appeared. We believe that the primary reason for this issue is the inability of stage 1 to establish a complete mesh. This difficulty arises from either the low input resolution or the overly concentrated viewing angles provided by the dataset. When the viewing angles are too concentrated, there is insufficient multi-angle information to accurately capture the full structure of the observed object. Consequently, this limitation prevents the formation of a closed mesh, which is essential for accurate modeling and subsequent optimization. As a result, the performance of our method is adversely affected on some data.

E Social Impact

Beyond entertainment, 3D simulation technology has significant implications for other sectors as well. In architecture and urban planning, it allows for the creation of detailed 3D models of buildings and cities, facilitating better design and decision-making. In healthcare, it can aid in surgical planning

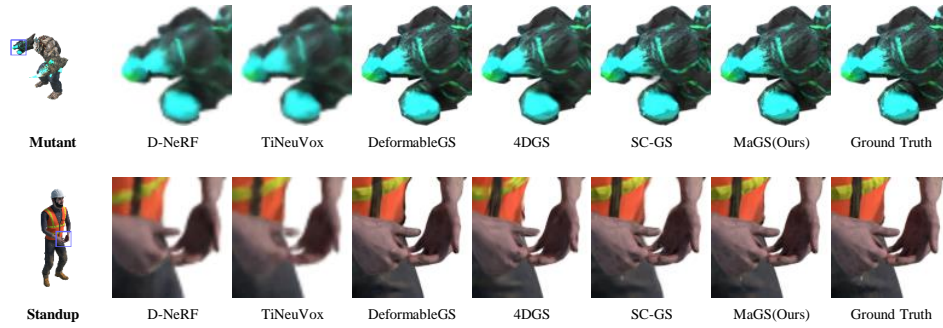


Figure 8: Qualitative comparison of dynamic view synthesis on the D-NeRF [33] dataset. We compare MaGS with D-NeRF [33], TiNeuVox-B [5], K-Planes [48], DeformableGS [48], 4D-GS [43], SC-GS [11].

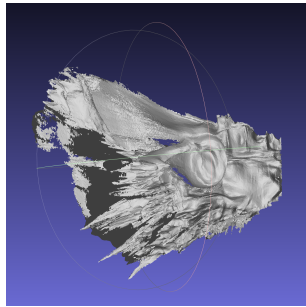


Figure 9: Unsatisfied Mesh in NeRF-DS [45]

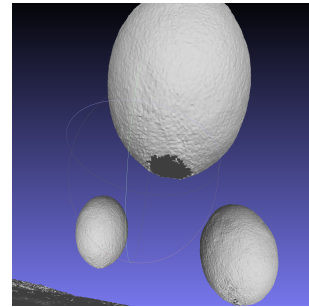


Figure 10: Unsatisfied Mesh in D-NeRF [33]

and medical training by simulating complex procedures or anatomical structures. In education, it can create interactive and immersive learning experiences, enhancing understanding and retention.

However, the power of 3D simulation technology also brings potential risks. The ability to generate realistic dynamic 3D content can be misused to create deepfakes - counterfeit videos or images that can deceive viewers into believing false information. This raises serious concerns about misinformation, privacy, and security. For instance, deepfakes could be used to spread fake news, manipulate public opinion, or commit fraud. Therefore, it is crucial to develop robust detection techniques and legal frameworks to mitigate these risks.